Software-Defined Radio-Based 5G Physical Layer Experimental Platform for Highly Mobile Environments

SHOTA MORI [1,2] **(Student Member, IEEE), KEIICHI MIZUTANI** [1] **(Member, IEEE), AND HIROSHI HARADA** [1] **(Member, IEEE)**

[1]Graduate School of Informatics, Kyoto University, Kyoto 606-8501, Japan
[2]School of Platforms, Kyoto University, Kyoto 606-8501, Japan

CORRESPONDING AUTHOR: HIROSHI HARADA (e-mail: hiroshi.harada@i.kyoto-u.ac.jp)

ABSTRACT In this study, we developed a 5th generation mobile communication (5G) physical layer (PHY) experimental platform based on software-defined radio (SDR), which makes it easy to customize the transmission and reception process. The developed platform consists of an SDR-based transmitter and a receiver. Digital baseband processing is performed using internal software-based programs. Therefore, it can be used to evaluate the wireless communication performance of 5G (or user-defined modified/customized 5G) not only in a laboratory but also in any field. In addition, as an example of the use of this platform, we proposed signal processing that can receive signals at speeds of 500 km/h or higher and performed an experimental evaluation by running it on the developed platform. Through laboratory experiments in a multipath fading environment using a fading emulator, performance of the developed platform was validated. Moreover, it was confirmed that this platform can satisfy the required block error rate of 0.1 even in a multipath environment at a velocity of approximately 630 km/h, which exceeds the requirements of 5G. Therefore, it has sufficient resilience to be used in high-moving-speed environments. This platform is expected to enable simple testing and evaluation of various new PHY technologies.

INDEX TERMS Highly mobile, software-defined radio, vehicular network, V2X, 5G.

I. INTRODUCTION

In recent years, mobility has been rapidly evolving. Intelligent transportation systems (ITS) and semi-automated car systems are becoming increasingly popular vehicular systems [1], [2], [3], and the era of fully autonomous driving will soon be upon us. In railway systems, ultra-high speeds are also being realized, with superconducting maglev in Japan achieving speeds of 603 km/h in 2015 [4]. Demonstrations of manned drone cab services are also underway [5]. Thus, we are approaching an era in which mobility with higher degrees of freedom and speeds will be realized. Wireless communications play an important role in this mobility revolution. For example, connected car systems require two types of wireless communication: short/middle-range communication for ITS and long-range and large-capacity communication for telematics services. ITS wireless communication consists of vehicle-

to-everything (V2X) communications, such as vehicle-to-vehicle (V2V), vehicle-to-infrastructure (V2I), vehicle-to-pedestrian (V2P), and vehicle-to-network (V2N) communications [6]. For V2X, several wireless communication standards have been developed, such as IEEE 802.11p [7], ARIB STD-T109 [8], and long-term evolution (LTE)-based V2X [9].

IEEE 802.11p was developed as a wireless access technology for V2V and V2I communications based on 802.11 standards operating in the 5.9 GHz band. This standard was developed mainly for the U.S. and Europe. The supporting data rate is 3–27 Mbps and the supporting communication distance is approximately 250 m [10], [11]. ARIB STD-T109 is another V2V and V2I communication system developed as a standard operating in the 760 MHz band. Originally, ARIB STD-T109 was a Japanese domestic standard and was agreed upon as one of the international standards at the World

Radiocommunication Conference (WRC) in 2019. Because the operating frequency of the ARIB STD-T109 is lower than that of IEEE 802.11p, a wider coverage (i.e., approximately 1 km) can be realized [11].

As a further wide-range V2X communication system, a study on the application of IEEE 802.22 (a wireless regional area network (WRAN) using television (TV) white spaces (TVWS) in very-high-frequency (VHF) and ultra-high-frequency (UHF)-bands) to mobility environments has been reported [12]. The coverage of IEEE 802.22 is 10–30 km, and the base station (BS) can connect up to 512 terminals.

The third-generation partnership project (3GPP) has also developed a wireless communication standard for V2X. 3GPP released LTE-based V2X, which is called LTE-V2X, within its Release-14 in 2016. LTE-V2X has a better power efficiency and introduces stronger channel coding than IEEE 802.11p [13]. In addition, resilience in a multipath environment is stronger owing to the longer symbol duration. Currently, to further improve end-to-end latency and capacity, the development of the 5th generation mobile communication (5G) new radio (NR)-based V2X (i.e., 5G NR-V2X) is underway [14]. It has been demonstrated that 5G NR-V2X is superior to other standards in terms of reliability, range, latency, and data rate [13]. Field experiments, such as the evaluation of V2V communication in the sub-6 GHz band for platooning in a highway environment, have been conducted [15].

However, 3GPP-based cellular systems will be increasingly used for telematics services that require long-range and large-capacity communications. In particular, the 5G NR operated in sub-6 GHz and millimeter wave bands allows for a flexible signal configuration because several numerologies are supported. Because three scenarios, namely enhanced mobile broadband (eMBB), ultra-reliable and low-latency communications (URLLC), and massive machine-type communications (mMTC), can be used adaptively according to the use cases in the 5G NR, it is expected to enable the development of various applications in the future [16]. In addition, 5G is required to support high-speed deployment scenarios of up to 500 km/h [17].

To support the ever-evolving means of mobility in various fields of land, sea, and air, various new physical layer (PHY) technologies need to be developed for 6G, including the development of transmission and reception methods that enable communication at speeds exceeding 500 km/h, new communication methods to enable many users to conduct high-capacity communication, and methods to achieve lower latency and more reliable communication (e.g., non-orthogonal multiple access (NOMA) [18], [19], [20], in-band full-duplex (IBFD) [21], [22], [23], and new waveforms [24], [25], [26], [27], [28]). However, many studies have been limited to numerical and simulation evaluations based on theoretical formulas or computer simulations, and there are significant barriers to actual device demonstrations. For example, in [29], a software-define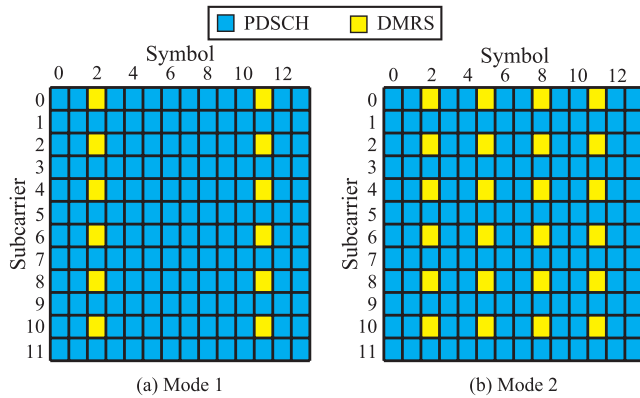d radio (SDR)-based prototype of user equipment (UE) supporting 4×4 multiple-input multiple-output (MIMO) in the sub-6 GHz band using five FPGAs was proposed. In [30], a platform for evaluating the communication performance in the sub-6 GHz band using SDR and a system-on-chip (SoC) was reported, which can transmit or receive LTE-based waveforms. However, these platforms are not generalized but application-specific evaluation platforms. For many researchers and engineers to easily experiment and evaluate new technologies, a general-purpose measurement platform that can be easily modified to transmit and receive signal processing of 5G PHY-based signals is needed. Moreover, considering that the transmission characteristics such as block error rate (BLER) are to be analyzed later, the platform should be able to acquire channel state information (CSI) as well as the transmission characteristics simultaneously.

In this study, we developed a 5G PHY experimental platform based on SDR that can easily customize the transmission and reception processes. The developed platform consists of an SDR-based transmitter and receiver. Digital baseband processing is performed using internal software-based programs. Therefore, it can be used to evaluate the wireless communication performance of 5G (or user-defined modified/customized 5G) not only in a laboratory but also in any field. The developed platform can acquire CSI and measure the associated BLER at that time. Therefore, it can contribute to the development of new access technologies and applications for 5G using CSI. Finally, as an example of the use of this platform, we proposed signal processing that can receive signals at speeds of 500 km/h or higher and performed an experimental evaluation by running it on the developed platform.

The main contributions of this study are summarized as follows:

- We developed a 5G transmitter/receiver PHY experimental platform using SDR. Because they are controlled and processed by software, the signal configuration and baseband signal processing can be easily changed.
- We propose a timing synchronization scheme using 5G synchronization signals that can be synchronized even at speeds of 500 km/h or higher. We also implement a carrier frequency offset (CFO) estimation and compensation scheme using a cyclic prefix (CP).
- The BLER performance of the proposed platform was measured through laboratory experiments using a fading emulator (FE). As a result, it is equivalent to that of a computer simulation, and a required BLER of 0.1 can be achieved even in a high-speed environment of 620 km/h.

The remainder of this paper is organized as follows: Section II explains the physical layer of the 5G system; Section III proposes 5G evaluation platforms; Section IV proposes reception processing of 5G digital baseband signals for high-speed mobility, including timing synchronization and CFO compensation schemes; Section V evaluates the performances of the proposed setups in the laboratory; and finally, Section VI concludes this paper.

FIGURE 1. Examples of resource allocation in 5G system.

FIGURE 2. Configuration of SSB.

TABLE 1. Resource Allocation of SSB

Channel or signal	Relative OFDM symbol number	Relative subcarrier number
PSS	0	56, 57, …, 182
SSS	2	56, 57, …, 182
Set to 0	0	0, 1, …, 55, 183, 184, …, 239
	2	48, 49, …, 55, 183, 184, …, 191
PBCH	1, 3	0, 1, …, 239
	2	0, 1, …, 47
		192, 193, …, 239
DMRS for PBCH	1, 3	$0 + v, 4 + v, 8 + v, …, 236 + v$
	2	$0 + v, 4 + v, 8 + v, …, 44 + v$
		$192 + v, 196 + v, 8 + v, …, 236 + v$

II. 5G PHYSICAL LAYER

A. OVERVIEW

We provide a brief explanation of 5G PHY. In the time domain, one frame has a fixed duration of 10 ms and is divided into ten equally-sized subframes of 1 ms duration [31]. The concept of the frame is the same as that of LTE, but that of the slot is different. 5G defines one slot as 14 orthogonal frequency-division multiplexing (OFDM) symbols. The subcarrier spacing is defined as $\Delta f = 2^{\mu} \cdot$ 15 [kHz] ($\mu = 0, \ldots, 4$). Therefore, the duration of one slot is dependent on the applied numerology, namely $1 / 2^{\mu}$ [ms]. Time-domain format of 5G is changeable for the capacity and latency requirement and the propagation environment.

5G defines consecutive subcarriers as a resource block (RB), which is the minimum unit for resource allocation to users in the frequency domain. One subcarrier, which RB consists of, is called a resource element (RE). Each RE can be assigned to a physical downlink shared channel (PDSCH), which is used for user-plane data transmission, and demodulation reference signals (DMRSs), which are used for channel estimation and equalization. Fig. 1 shows examples of DMRS allocation in 5G networks. The DMRS arrangement styles can be flexibly changed depending on the assumed environment, such as the moving speed of the terminal. One slot can contain 1–4 OFDM symbols with DMRSs [31]. Therefore, Fig. 1(b), which contains four DMRS symbols (called Mode-2 in this paper), is more tolerant of a fast-moving environment than Fig. 1(a), which contains two DMRS symbols (called Mode-1).

B. SYNCHRONIZATION SIGNALS

For the initial access of terminals, cell identification (ID) detection, and timing synchronization point detection, two synchronization signals (SSs)—primary SS (PSS) and secondary SS (SSS)—are transmitted periodically from a base station (BS) [31], [32]. These signals are treated with the physical broadcast channel (PBCH) used to obtain basic information, such as the downlink (DL) system bandwidth and frame number and the DMRS for PBCH and SS/PBCH (SSB).
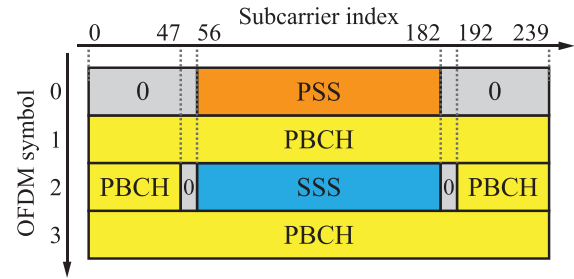
The configuration of the SSB in the time and frequency domains is shown in Fig. 2 and Table 1, where $v = N_{\text{cell}}^{\text{ID}}$ mod 4. The SSB consists of 240 subcarriers and four OFDM symbols (i.e., $20 \times 4 = 80$ RBs). The PSS and SSS sequences are defined according to the physical cell ID (PCI), $N_{\text{cell}}^{\text{ID}}$, calculated as follows:

$$N_{\text{cell}}^{\text{ID}} = 3N_{\text{ID}}^{(1)} + N_{\text{ID}}^{(2)}, \tag{1}$$

where $N_{\text{ID}}^{(1)} \in \{0, 1, \ldots, 355\}$ and $N_{\text{ID}}^{(2)} \in \{0, 1, 2\}$. The PSS is generated by modulating 128 bits of the M-sequence corresponding to $N_{\text{ID}}^{(2)}$ with BPSK modulation. Meanwhile, the SSS consists of BPSK symbols arising from a 128 bits gold sequence corresponding to $N_{\text{ID}}^{(1)}$. Therefore, terminals calculate PCI from a combination of three M-sequences and 356 gold sequences using SSB.

One or more SSBs are transmitted periodically by the BS within the half-frame (i.e., an SS burst). The periodicity of the SS burst, T_{SS}, was determined from $T_{\text{SS}} \in \{5, 10, 20, 40, 80, 160\}$ ms in the upper layer [33]. The maximum number of SSBs contained in one SS burst, $L_{\text{SSB}}^{\text{max}}$, was defined according to the frequency bands, f_{c}. When $f_{\text{c}} \leq 3$ GHz, 3 GHz $< f_{\text{c}} \leq 6$ GHz, and 6 GHz $< f_{\text{c}} \leq 52.6$ GHz, $L_{\text{SSB}}^{\text{max}}$ was 4, 8, and 64, respectively. The position of the first symbol of the SSB in the time domain is determined according to the frequency bands and subcarrier spacing, as listed in Table 2 [32]. Because each SSB is mapped to each beam, the detection of the SSB index, which is defined for each SSB in ascending order from zero, is also used for beam management.

In this study, to develop a prototype for evaluating wireless communication performance, we assume that PSS and SSS sequences, PCI, periodicity of SS burst, number of SSBs in

TABLE 2. SSB Position in the Time Domain

Case	Subcarrier spacing [kHz]	Candidate indexes of first symbol for SSB
A	15	$\{2,8\} + 14n$
		when $f_c \leq 3$ GHz, $n = 0, 1$
		when 3 GHz $< f_c \leq 6$ GHz, $n = 0, 1, 2, 3$
B	30	$\{4,8,16,20\} + 28n$
		when $f_c \leq 3$ GHz, $n = 0$
		when 3 GHz $< f_c \leq 6$ GHz, $n = 0, 1$
C	30	$\{2,8\} + 14n$
		when $f_c \leq 3$ GHz, $n = 0, 1$
		when 3 GHz $< f_c \leq 6$ GHz, $n = 0, 1, 2, 3$
D	120	$\{4,8,16,20\} + 28n$
		when $f_c > 6$ GHz,
		$n = 0,1,2,3,5,6,7,8,10,11,12,13,15,16,17,18$
F	240	$\{8,12,16,20,32,36,40,44\} + 56n$
		when $f_c > 6$ GHz, $n = 0,1,2,3,5,6,7,8$

FIGURE 4. Block diagram of 5G baseband signal generation.
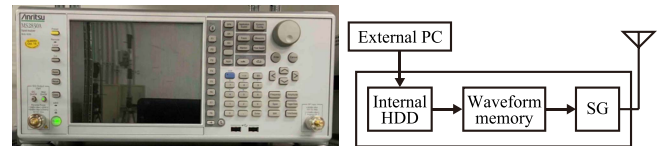
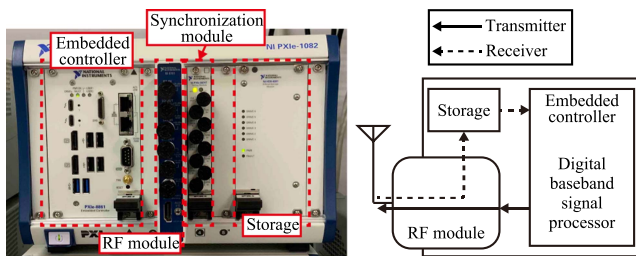**FIGURE 5.** Configuration of SG-based 5G transmitter.

FIGURE 3. Configuration of SDR-based 5G transmitter and receiver.

one SS burst, and position of SSB are fixed and already known to UEs. In addition, all the SSBs are assumed to be transmitted from the same antenna.

III. PROPOSED EXPERIMENTAL MEASUREMENT PLATFORM

In this section, we propose a flexible experimental measurement platform for 5G PHY using SDR. This prototype is assumed to be a BS, which transmits a DL signal, and a UE, which receives a DL signal, and can evaluate the DL communication performance of 5G.

A. SOFTWARE-DEFINED RADIO-BASED TRANSMITTER

Fig. 3 shows the configuration of the developed SDR-based 5G transmitter. The RF module (5791, National Instruments (NI)) connected to an FPGA module (PXIe-7975R, NI), synchronization module (PXIe-6674T, NI), data storage module (HDD-8261, NI), and embedded controller (PXIe-8861, NI) were installed in a chassis with a high-speed local bus (PXIe-1082, NI). The RF module supports a frequency range from 200 MHz to 4.4 GHz and a bandwidth of up to 100 MHz. Therefore, this SDR-based transmitter is suitable for evaluating the 5G PHY performance in the sub-6 GHz. The accuracy of the 10 MHz reference clock of the chassis is ± 25 ppm [34]. However, it does not meet the frequency error minimum requirement of BS, ± 0.05 ppm for the wide area BS and ± 0.1 ppm for the medium range and the local area BS [35]. Thus, a reference clock generated by the synchronization module,
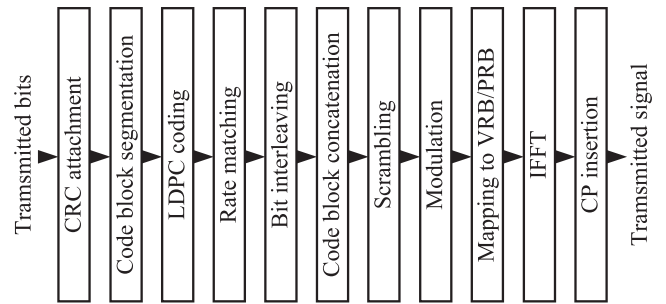
whose initial accuracy of OCXO is ± 0.08 ppm, is used [36]. This clock is shared by all the modules via the high-speed local bus of the chassis.

Fig. 4 shows a block diagram of the 5G digital baseband signal generation. Because all these processes, such as low-density parity-check (LDPC) coding and modulation, are performed by signal processing software (LabVIEW, NI and MATLAB, Mathworks) in the embedded controller, we can flexibly customize the parameters of 5G transmitting signals, such as subcarrier spacing, bandwidth, modulation and coding scheme (MCS), and DMRS configuration. The RF module converts the digital in-phase and quadrature (I/Q) digital signal into an analog signal using a 16-bit digital-to-analog converter (DAC), upconverts it to the RF analog signal, and continuously transmits the signal through a subminiature type A (SMA) connector. Field experiments can be conducted easily by connecting the antenna to the RF module.

B. SIGNAL GENERATOR-BASED TRANSMITTER

To validate the developed SDR-based transmitter, a signal generator (SG)-based 5G transmitter was set up. Fig. 5 shows the configuration of the SG-based 5G transmitter. The SG (MS2830A, Anritsu) can transmit an arbitrary 5G signal, which is imported from an external control PC processing the 5G signal generation, as shown in Fig. 4, via an Ethernet interface or stored internally. The SG supports a frequency range of 250 kHz–6 GHz and a bandwidth of up to 120 MHz. In addition, 14-, 15-, and 16-bits waveform resolutions are supported. The SG upconverts the baseband signal to an RF signal and outputs it via an SMA connector. However, this SG-based transmitter is not suitable for field experiments for two reasons. First, it needs an external control PC to flexibly change the baseband signal waveforms. Second, because the accuracy of the reference clock is unclassified, a CFO may occur if the reference clock of the transmitter is not shared with the receiver.
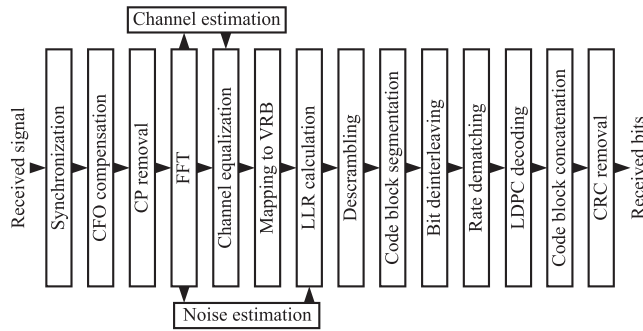
FIGURE 6. Block diagram of the proposed 5G baseband signal reception processor.

C. SOFTWARE-DEFINED RADIO-BASED RECEIVER

The configuration of the SDR-based receiver was the same as that of the SDR-based transmitter, as shown in Fig. 3. The RF module down-converts the received RF signal to a baseband signal, and converts it to an I/Q digital signal using a 14-bit analog-to-digital converter (ADC). The quantization bit of the converted digital signal is changed to 16-bit by signal processing implemented on the FPGA module and then stored as technical data management streaming (TDMS) files. Afterward, the embedded controller converts the TDMS files to comma-separated value (CSV) files using signal processing software (LabVIEW), and performs reception processing, as shown in Fig. 6, using signal processing software (MATLAB). As with the SDR-based transmitter, this receiver uses the reference clock generated by not the chassis but the synchronization module because the frequency error minimum requirement of UE is defined as ±0.1 ppm [37].

The default RF/FPGA module was not equipped with an automatic gain control (AGC) function. Therefore, we implemented a quasi-real-time AGC that works through the coordination of software-based signal processing and an RF/FPGA module. In this development platform, a quasi-real-time AGC function is achieved by increasing or decreasing the reference level (dBm) for the reception of the RF module (i.e., input level to the ADC) in 1 dB steps. This is performed according to the maximum amplitude calculated from the I/Q 16-bit signed integer extracted from 1000 samples every 10 ms. Here, this amplitude takes a value from 0 to 46341. The threshold values for the decrement and increment were set to 13044 and 26027, respectively. All judgement results are stored in CSV files with time stamps to allow reference to the true received power.

IV. PROPOSED RECEPTION PROCESSING OF 5G DIGITAL BASEBAND SIGNAL FOR HIGH-SPEED MOBILITY

As an example of the use of this platform explained in Section III, we propose signal processing that can receive signals at speeds of 500 km/h or higher and perform an experimental evaluation by running it on the developed platform. Specifically, we propose a signal-synchronization method and a CFO

estimation method. Fig. 6 shows a block diagram of the proposed reception process for high-speed mobility.

A. TIMING SYNCHRONIZATION

Firstly, the receiver must perform timing synchronization to start reception processing. In this study, a timing synchronization algorithm based on cross-correlation [38] using SSB was introduced into the SDR-based receiver. First, a standby signal, x_{sb}, was generated. The BPSK symbols generated by known PSS and SSS sequences are mapped into the frequency domain to the RBs where PSS and SSS are allocated. Zero is mapped to the RBs where they are not allocated. Then, the time-domain signals, $x_{PSS}[n']$ and $x_{SSS}[n']$ ($n' = 0, \ldots, N_{FFT} + L - 1$), are obtained through inverse fast Fourier transform (IFFT) and CP insertion processes, where N_F is the IFFT size and L is the CP length. Because there is one OFDM symbol between the PSS and SSS in the time domain, we obtain $x_{sb}[n'']$ as follows:

$$x_{sb}\left[n''\right] = \begin{pmatrix} x_{PSS} & 0_{1 \times (N_F+L)} & x_{SSS} \end{pmatrix},$$
$$\left(n'' = 0, \ldots, 3\left(N_F + L\right) - 1\right), \tag{2}$$

where $0_{A \times B}$ denotes an $A \times B$ size zero matrix.

Second, the cross-correlation between the received digital signal $r[n]$, and the standby signal is calculated as

$$x_1\left[n\right] = \left| \sum_{m=0}^{3(N_F+L)-1} r\left[n+m\right] x_{sb}^*\left[m\right] \right|, \tag{3}$$

where $(\cdot)^*$ denotes the complex conjugate. To suppress the variation in the $x_1[n]$ owing to the channel time variation, the moving averaging of $x_1[n]$, x_1^{Ave}, and the ratio of x_1 to x_1^{Ave}, x_2, are calculated as follows:

$$x_1^{Ave}\left[n\right] = \frac{1}{2M_1 + 1} \sum_{m=-M_1}^{M_1} x_1\left[n+m\right], \tag{4}$$

$$x_2\left[n\right] = \frac{x_1\left[n\right]}{x_1^{Ave}\left[n\right]}, \tag{5}$$

where $M_1 = 2L$ is the moving averaging window size. As mentioned above, because there are n_{SSB} ($1 \leq n_{SSB} \leq L_{SSB}^{max}$) SSBs exist in the SS burst, the peaks in $x_2[n]$ appear n_{SSB} times. In addition, the spacing of the peaks can be determined from the positions of the OFDM symbols containing SSBs. Therefore, to improve the detection ratio of the first SSB, $x_2[n]$ is added so that the peaks overlap, as follows:

$$x_3\left[n\right] = \sum_{i=1}^{n_{SSB}} x_2\left[n + (S_i - S_1)(N_F + L)\right], \tag{6}$$

where S_i (≥ 0) is the first OFDM symbol index of the ith ($i = 1, \ldots, n_{SSB}$) SSB during the SS burst.

Finally, the synchronization point p, which is the first time-sample index of the slot containing the first SSB, is calculated

as follows:

$$p = \operatorname*{argmax}_{m \in [n-M_2, n+M_2]} (x_3[m]) - S_1(N_F + L), \quad (7)$$

$$\text{s.t.} \quad x_3[n] \geq \alpha x_3^{\mathrm{Ave}}[n] \quad (8)$$

where

$$x_3^{\mathrm{Ave}}[n] = \frac{1}{2M_1 + 1} \sum_{m=-M_1}^{M_1} x_3[n+m], \quad (9)$$

where α is the threshold value for peak detection and $M_2 = n_{\mathrm{SSB}}^{\mathrm{slot}}(N_F + L)N_{\mathrm{symb}}^{\mathrm{slot}}$ is the window length for the determination of the maximum peak. $n_{\mathrm{SSB}}^{\mathrm{slot}}$ and $N_{\mathrm{symb}}^{\mathrm{slot}}$ ($= 14$) denote the number of slots containing SSB in the SS burst and OFDM symbols in a slot, respectively. α should be set appropriately because (8) is essential for detecting the peak and not for detecting the data slot.

B. CARRIER FREQUENCY OFFSET ESTIMATION
As mentioned above, in 5G, both BS and UE must have high-frequency accuracy of ± 0.1 ppm, but CFO may be high in a high-speed environment owing to the Doppler shift, which deteriorates the communication quality. Therefore, to estimate and compensate the CFO in a very high mobility environment (i.e., more than 500 km/h), an autocorrelation-based CFO compensation algorithm [39] was applied to the SDR-based receiver. The estimated CFO value, $\hat{f}_{\mathrm{CFO}}$, was calculated as

$$\hat{f}_{\mathrm{CFO}} = \frac{1}{2\pi N_F t_{\mathrm{s}}} \arg \left\{ \sum_{q=0}^{Q-1} \sum_{l=0}^{L-1} x\left[p + q(N_F + L) + l\right] \right.$$
$$\left. \cdot x^*\left[p + q(N_F + L) + l + N_F\right] \right\}, \quad (10)$$

where t_{s} is the sampling interval of the baseband signal and $Q = \left(n_{\mathrm{SSB}}^{\mathrm{slot}} + n_{\mathrm{Data}}^{\mathrm{slot}}\right) N_{\mathrm{symb}}^{\mathrm{slot}}$ is the number of OFDM symbols considered in the CFO estimation. $n_{\mathrm{Data}}^{\mathrm{slot}}$ denotes the number of slots that do not contain the SSB. After the CFO calculation, the CFO is removed from the received signal as:

$$\hat{x}[n_{\mathrm{r}}] = x[n_{\mathrm{r}}] \mathrm{e}^{j 2\pi \hat{f}_{\mathrm{CFO}} n_{\mathrm{r}} t_{\mathrm{s}}}, \quad (11)$$

where $n_{\mathrm{r}} = n - p$ is the relative time-sample index from the synchronization point of the received baseband signal. This scheme can compensate for the CFO by up to half of the subcarrier spacing.

After CFO compensation, the reception processes, such as channel estimation and equalization using the DMRS, linear interpolation/extrapolation, and LDPC decoding using the log-domain sum-product algorithm, are executed.

V. EXPERIMENTAL SETUP AND EVALUATION RESULTS
In this section, we describe the experimental setup in a laboratory and demonstrate the effectiveness of the proposed SDR-based transmitter and receiver in a high-speed mobility environment using an FE.
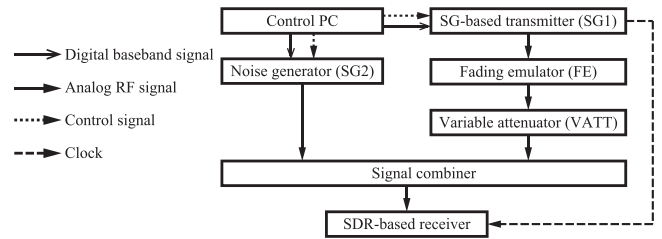

FIGURE 7. Configuration of the SG-SDR platform.

TABLE 3. Equipment List

Equipment	Product model
SG1	MS2830A, Anritsu
SG2	MS2830A, Anritsu
Variable attenuator (VATT)	8494A, Keysight
	8496B, Keysight
Signal combiner	PD510-0S, R&K
SDR devices	
・Chassis	PXIe-1082, NI
・Embedded controller	PXIe-8861, NI
・RF adapter module	5791, NI
・FPGA module	PXIe-7975R, NI
・Synchronization module	PXIe-6674T, NI
・Storage module	HDD-8261, NI
Fading emulator	NJZ-1600D, JRC
Baseband signal processor	
・SDR devices	MATLAB 2021b, Mathworks
・Control PC	MATLAB 2017b, Mathworks
Control PC	Probook 450 G3, HP
	(Intel Core i7-6500U CPU, 8G RAM)

A. EVALUATION SETUP FOR PLATFORM WITH SG-BASED TRANSMITTER AND SDR-BASED RECEIVER
The first setup of the platform consists of an SG-based transmitter and an SDR-based receiver. This setup is hereafter referred to as the SG-SDR platform. Fig. 7 shows the structure of the SG-SDR platform. The used equipment is presented in Table 3. The baseband 5G signal generated by MATLAB in the control PC was converted to WVI and WVD files using the software provided by Anritsu and transported to the first SG (SG1) via a 1000BASE-T Ethernet cable. In addition, parameter sets, such as the carrier frequency and sampling rate, were sent to SG1. SG1 then transmits the RF signal, which is the upconverted signal of the generated 5G signal.

The transmitted RF signal was fed into the FE (JRC, NJZ-1600D) via an RF coaxial cable. The faded signal was attenuated by variable attenuators (VATTs) and combined with additive white Gaussian noise (AWGN) generated by the second SG (SG2). The contaminated RF signal is then fed into the SDR-based receiver.

The SDR-based receiver records the baseband signal as a TDMS file using LabVIEW-based signal recording program software in the embedded PC. The recorded signal was converted to CSV files and processed as mentioned in Section III using MATLAB-based demodulation software.

To utilize this SG-SDR platform for evaluation without the impact of the CFO, the 10 MHz reference clock generated
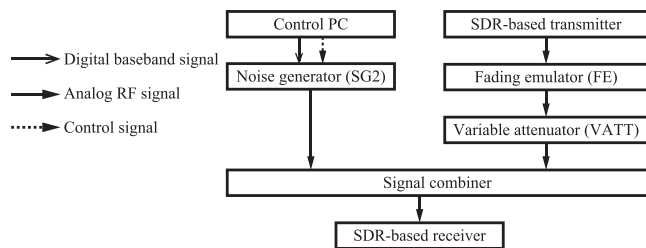
FIGURE 8. Configuration of SDR-SDR evaluation setup.

TABLE 4. The Delay Profile of Modified EVA Model

Path	1	2	3	4	5	6
Delay [ns]	0	30	150	370	1090	2510
Relative power [dB]	0.0	−1.5	−1.4	−0.6	−7.0	−16.9

in SG1 is fed into the SDR-based receiver to synchronize the clock. Therefore, the CFO compensation scheme is not executed during the reception process.

B. EVALUATION SETUP FOR PLATFORM WITH SDR-BASED TRANSCEIVER

The second setup of the platform consists of an SDR-based transmitter and receiver. This setup is hereafter referred to as the SDR-SDR platform. Fig. 8 shows the structure of the SDR-SDR platform. The used equipment is also listed in Table 3, which is almost the same as that of the SG-SDR platform.

The SDR-based transmitter generates a baseband 5G signal using MATLAB and transmits an RF signal. The other operations of the SDR-SDR platform were the same as those of the SG-SDR platform. In this setup, because the 10 MHz reference clock is not shared between the SDR-based transmitter and receiver, the CFO compensation scheme described in Section IV is executed.

C. PROPAGATION CHANNEL

In this study, NJZ-1600D, JRC, was used as the FE to evaluate communication performance in a multi-path high-speed fading environment. This FE can emulate two 6-path channels (i.e., up to 12 paths) and supports frequency ranges from 70 MHz to 340 MHz, 460 MHz to 3 GHz, and a maximum bandwidth of 20 MHz. The maximum Doppler frequency was set to 2 kHz. Because of the limited number of paths that can be configured for the FE used in this study, we use a channel model in which the number of taps in the 9-tap EVA (extended vehicular A (EVA) channel model provided by 3GPP [40] is reduced to the six taps shown in Table 4 (referred to as the modified EVA model in this paper). Each path was faded by Rayleigh fading.

D. PARAMETERS AND FRAME STRUCTURE

Parameters of the 5G baseband signal and evaluation setup are listed in Table 5. The frequency range and channel bandwidth are set to 2.15 GHz and 20 MHz, respectively. In this

TABLE 5. Evaluation Parameters

Parameter	Value
Channel bandwidth	20 MHz
Subcarrier spacing	15 kHz
Allocated bandwidth	106 PRBs
FFT size	2,048
CP rate	144/2,048 (all symbols)
Sampling rate	30.688 MHz
Coding scheme	LDPC
Modulation Scheme,	MCS7 (QPSK), $R = 526/1,024$
Code Rate R	MCS13 (16QAM), $R = 490/1,024$
Transport block size	MCS7: 2,112 bytes
	MCS13: 3,969 bytes
Decoding algorithm	Log-domain sum-product
Decoding iteration	50
Carrier frequency	2.15 GHz
Channel	modified EVA
Moving speed	80 km/h (159.3 Hz)
Antenna	Tx: 1, Rx, 1
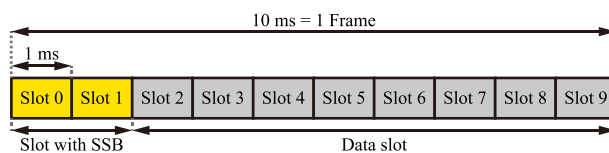
FIGURE 9. Frame configuration.

study, QPSK (MCS7) and 16QAM (MCS13) modulations were used to evaluate communication quality. As shown in Fig. 1, two DMRS configurations were evaluated: Mode-1 with two OFDM symbols containing DMRS and Mode-2 with four OFDM symbols containing DMRS in one slot. However, unless specifically mentioned, Mode-1 was used in this study. The frame configuration is shown in Fig. 9. Assuming $T_{SS} = 10$ ms, one frame consisting of 10 slots is repeatedly sent. The first two slots contain two SSBs (i.e., $n_{SSB}^{slot} = 2$ and $n_{SSB} = 4$), and the rest are data slots (i.e., $n_{Data}^{slot} = 8$). In this study, only the data slots were considered for evaluating communication quality.

E. COEFFICIENT DECISION BY COMPUTER SIMULATION

Prior to evaluation using the actual developed platforms, the coefficient α in (8), which is crucial for precise timing synchronization, must be determined by computer simulations. In contrast to actual platforms, we can determine the approximate synchronization point in a computer simulation. Therefore, the cross-correlation between x_{sb} and the first half of the first slot (i.e., slot 0 shown in Fig. 9) was calculated, and a pseudo-synchronization point, P_{psp}, was obtained as follows:

$$P_{psp} = \operatorname*{argmax}_{m \in [0, 7(N_F + L)]} \left| \sum_{m=0}^{3(N_F + L) - 1} x[n + m] x_{SB}^*[m] \right|. \quad (12)$$

Then, the cumulative distribution functions (CDFs) of $x_3[P_{psp}]/x_3^{Ave}[P_{psp}]$ are shown in Fig. 10 in the case of signal-to-noise power ratio (SNR) of 5 dB. We also show the CDF of x_3/x_3^{Ave} in data slot 4, so that the data slot cannot satisfy (8).
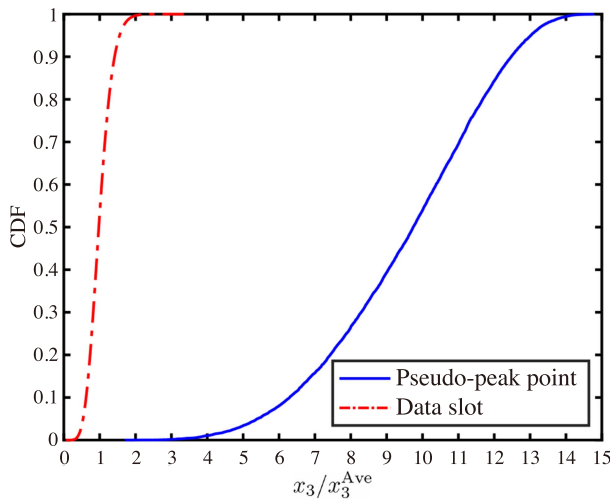
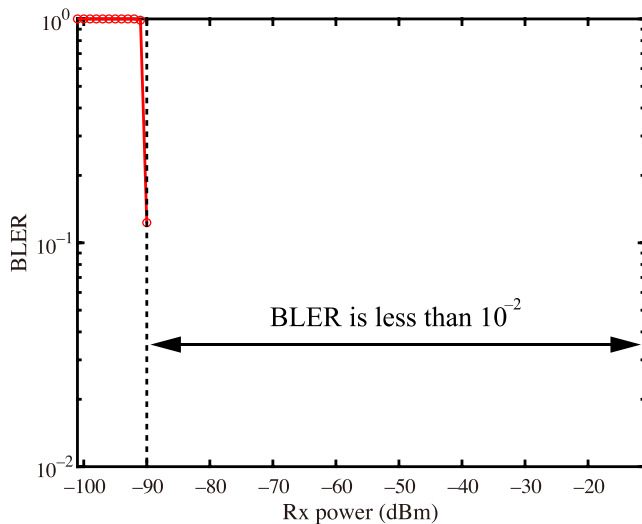FIGURE 10. CDF of x_3/x_3^{Ave} in the case of SNR = 5 dB.

FIGURE 11. Dynamic range of the SDR-based receiver.

The impact of CFO was not considered in this simulation. As a result, when $\alpha = 4$, the data slots cannot satisfy (8), resulting in a 99% pseudo-ideal point. Therefore, in this study, $\alpha = 4$ is used in subsequent evaluations.

F. DYNAMIC RANGE OF THE SDR-BASED RECEIVER
To evaluate the dynamic range of the SDR-based receiver, BLER characteristics were evaluated using the SG-SDR platform without fading and noise. The transmit (Tx) power of the SG-based transmitter was set to –5 dBm and VATT was set from 0 dB to 90 dB. Fig. 11 shows the BLER characteristics with QPSK modulation (MCS7) as a function of a receive (Rx) power from –101.0 dBm to –11.0 dBm. The BLER is less than 10^{-2} between –89.0 dBm and –11.0 dBm. Therefore, the dynamic range of the SDR-based receiver is greater than 78 dB. Because the Tx power is generally attenuated up to 40 dB in a multipath fading environment, the Tx powers of the
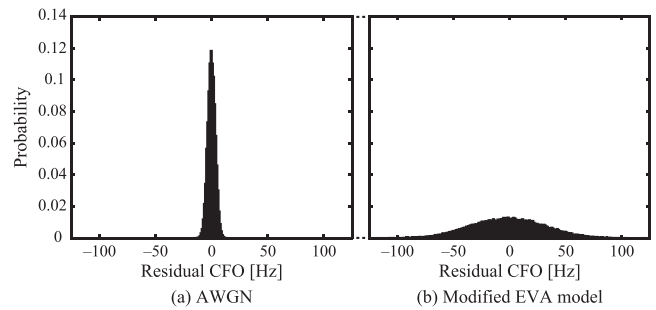

FIGURE 12. Residual CFO.

SG-based transmitter and the SDR-based transmitter are set to –30 dBm and –20 dBm, respectively.

G. CFO COMPENSATION PERFORMANCE EVALUATION
The implemented CFO compensation scheme is evaluated using the SG-SDR platform. To fix the value of CFO generated by the frequency error between the transmitter and receiver, frequency offsets of +0.1 ppm and –0.1 ppm are given to the SG-based transmitter and SDR-based receiver, respectively. Thus, the value of the CFO is 430 Hz. Fig. 12 shows the histogram with a bin width of 1 Hz of the residual CFO value calculated by subtracting $\hat{f}_{\text{CFO}}$ from 430 Hz for SNR = 15 dB. Fig. 12(a) and (b) illustrate the results under the AWGN environment without using FE and the multipath fading environment at a velocity of 80 km/h. In an AWGN environment, the CFO is sufficiently reduced, its standard deviation is 3.4 Hz and 99.7% of the residual CFO is less than 10 Hz. On the other hand, in a multipath fading environment, the performance of the CFO compensation scheme deteriorates owing to channel time variation. However, because the standard deviation is 31.4 Hz and 99.7% of the residual CFO is less than 87 Hz, the implemented CFO compensation scheme is sufficiently effective.

H. BLER PERFORMANCE EVALUATION AS A FUNCTION OF SNR
Fig. 13 shows the BLER performances of the SG-SDR and SDR-SDR platforms as a function of the SNR in the multipath fading environment. In addition, the BLER performance of the computer simulation with perfect timing synchronization and without CFO is shown for comparison. In this evaluation, both the QPSK (MCS7) and 16QAM (MCS13) were used. As a result, the performances of the actual platforms are equivalent to that of the simulation regardless of the MCS, although degradations within approximately 0.8 dB are present. It is considered that these degradations are caused by imperfections such as phase noise and the nonlinearity of the power amplifier. Therefore, we can see that the proposed timing-synchronization scheme works well. Moreover, because the results of the SDR-SDR platform are similar to those of the SG-SDR platform, the implemented CFO compensation scheme is sufficiently effective.
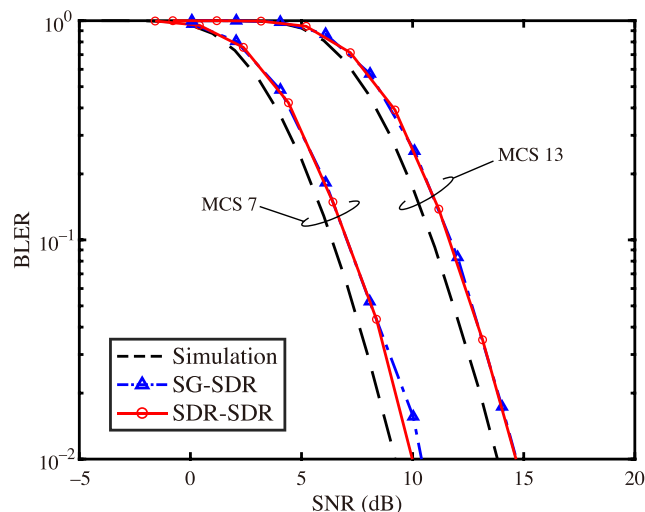
FIGURE 13. BLER characteristics of the SG-SDR and SDR-SDR platforms as a function of SNR.
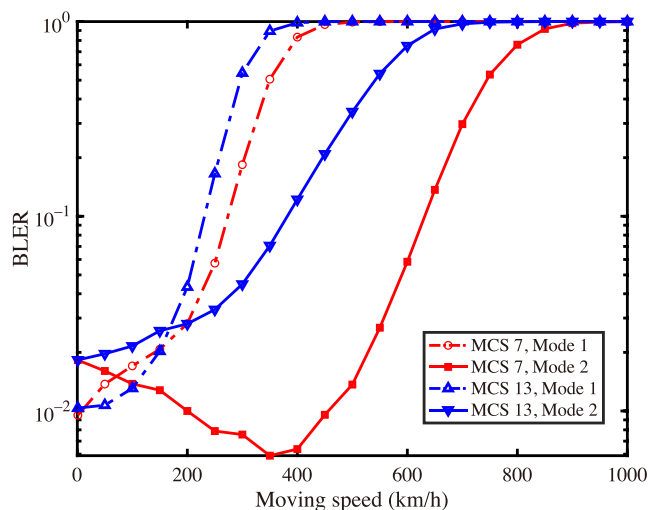

FIGURE 14. BLER characteristics of the SDR-SDR evaluation setups as a function of the moving speed.

I. BLER PERFORMANCE EVALUATION AS A FUNCTION OF TERMINAL MOVING SPEED

To evaluate the resilience to the moving speed of the UE, Fig. 14 shows the BLER performance as a function of the terminal moving speed using the SDR-SDR platform. QPSK (MCS7) and 16QAM (MCS13) modulation schemes with both Mode-1 and Mode-2, are used in the case of SNR = 9.5 dB and 14.5 dB. In this evaluation, we assumed that the required BLER was 10^{-1}. Broadly speaking, as the moving speed increases, the BLER performance deteriorates owing to an increase in the channel estimation error. Regarding the QPSK modulation, the required BLER is achieved up to approximately 270 km/h when Mode-1 is applied. However, using Mode-2, it was achieved up to approximately 630 km/h. Therefore, the DMRS configuration should change depending

on the moving speed and required BLER. Here, using QPSK modulation with Mode-2, the BLER decreased as the moving speed increased from 50 km/h to 350 km/h. When the moving speed is slow, the Rx power level may degrade throughout the slot. By contrast, in a high-moving speed environment, the channel estimation error becomes high, but the Rx power level fluctuates in the slot. Therefore, only when simple modulation schemes of low MCS are used, LDPC coding can correct the error caused by the low-power symbol using the high-power symbol. Therefore, a trade-off between the channel estimation error and the advantage of power fluctuation is considered, as shown in Fig. 14. For the 16QAM modulation with Mode-1 and Mode-2, the required BLER was achieved up to approximately 230 and 380 km/h, respectively. The resilience to moving speed is weaker than that of QPSK modulation, but 16QAM modulation can be sufficiently utilized in high-moving environments such as V2X or telematics communications.

The above results show that the wireless communication performance can be evaluated by changing the DMRS configuration and MCS, even in a high-moving speed environment up to approximately 630 km/h. Thus, the proposed SDR-SDR platform can easily perform flexible evaluations, such as robustness evaluation for high-speed mobility environments.

VI. CONCLUSION

In this study, we developed a 5G PHY experimental platform based on SDR that can easily customize the transmission and reception processes. The developed platform consists of an SDR-based transmitter and receiver. Digital baseband processing is performed using internal software-based programs. Therefore, it can be used to evaluate the wireless communication performance of 5G (or user-defined modified/customized 5G) not only in a laboratory but also in any field. In addition, as an application of this platform, we proposed signal processing that can receive signals at speeds of 500 km/h or higher (i.e., timing synchronization and CFO estimation and compensation) and performed an experimental evaluation by running it on the developed platform. Through laboratory experiments in a multipath fading environment using FE, the BLER performance of the developed SDR-based platform was proved to be equivalent to that of the computer simulation. Moreover, it was confirmed that this platform can satisfy the required BLER of 0.1 even in a multipath environment at a velocity of approximately 630 km/h, which exceeds the requirements of 5G. Thus, it has sufficient resilience to be used in a high-moving speed environment. Field experiments can be simply conducted using the developed platform because it is portable and can adjust/change parameters, such as the DMRS configuration, MCS, and subcarrier spacing. This platform is expected to enable simple testing and evaluation of various new PHY technologies.

REFERENCES

[1] X. Cheng, L. Yang, and X. Shen, "D2D for intelligent transportation systems: A feasibility study," *IEEE Trans. Intell. Transp. Syst.*, vol. 16, no. 4, pp. 1784–1793, Aug. 2015.

[2] T. V. Saraiva, C. A. V. Campos, R. R. Fontes, C. E. Rothenberg, S. Sorour, and S. Valaee, "An application-driven framework for intelligent transportation systems using 5G network slicing," *IEEE Trans. Intell. Transp. Syst.*, vol. 22, no. 8, pp. 5247–5260, Aug. 2021.

[3] T. Alladi, B. Gera, A. Agrawal, V. Chamola, and F. R. Yu, "DeepADV: A deep neural network framework for anomaly detection in VANETs," *IEEE Trans. Veh. Technol.*, vol. 70, no. 11, pp. 12013–12023, Nov. 2021.

[4] Central Japan Railway Company, "The review: Superconducting maglev (SCMAGLEV)," May 2017. [Online]. Available: https://global.jr-central.co.jp/en/company/_pdf/superconducting_maglev.pdf

[5] R. Kellermann, T. Biehle, and L. Fischer, "Drones for parcel and passenger transportation: A literature review," *Transp. Res. Interdiscipl. Perspectives*, vol. 4, pp. 1–13, Mar. 2020.

[6] L. Yang and F. Wang, "Driving into intelligent spaces with pervasive computing and communications," *IEEE Intell. Syst.*, vol. 22, no. 1, pp. 12–15, Jan./Feb. 2007.

[7] *Wireless LAN Medium Access Control (MAC) and Physical Layer (PHY) Specifications Amendment 6: Wireless Access in Vehicular Environments*, IEEE Standard 802.11p-2010, 2010.

[8] ARIB, "700 MHz band intelligent transport systems," ARIB STD-T109-v1.3, Jul. 2017.

[9] 3GPP, "Study on LTE-based V2X services (v14.0.0, release 14)," 3GPP Tech. Rep. 36.885, Jul. 2016.

[10] G. Cecchini, A. Bazzi, B. Masini, and A. Zenella, "Performance comparison between IEEE 802.11p and LTE-V2V in-coverage and out-of-coverage for cooperative awareness," in *Proc. IEEE Veh. Netw. Conf.*, 2017, pp. 109–114.

[11] J. Heinovski, F. Klingler, F. Dressler, and C. Sommer, "Performance comparison of IEEE 802.11p and ARIB STD-T109," in *Proc. IEEE Veh. Netw. Conf.*, 2016, pp. 1–8.

[12] R. Ouyang, T. Matsumura, K. Mizutani, and H. Harada, "Software-defined radio-based evaluation platform for highly mobile IEEE 802.22 system," *IEEE Open J. Veh. Technol.*, vol. 3, pp. 167–177, 2022.

[13] W. Anwar, N. Franchi, and G. Fettweis, "Physical layer evaluation of V2X communications technologies: 5G NR-V2X, LTE-V2X, IEEE 802.11bd, and IEEE 802.11p," in *Proc. IEEE Veh. Technol. Conf.*, 2019, pp. 1–7.

[14] 3GPP, "Study on NR vehicle-to-everything (V2X) (v16.0.0, release 16)," 3GPP Tech. Rep. 26.985, Mar. 2019.

[15] M. Mikami, K. Serizawa, Y. Ishida, H. Nishiyori, K. Moto, and H. Yoshino, "Field experimental evaluation on latency and reliability performance of 5G NR V2V direct communication in real express highway environment," in *Proc. IEEE Veh. Technol. Conf.*, 2020, pp. 1–5.

[16] A. Ghosh, A. Maeder, M. Baker, and D. Chandramouli, "5G evolution: A view on 5G cellular technology beyond 3GPP release 15," *IEEE Access*, vol. 7, pp. 127639–127651, 2019.

[17] 3GPP, "Service requirements for the 5G system," 3GPP Tech. Specification 22.261.

[18] G. Liu, Z. Wang, J. Hu, Z. Ding, and P. Fan, "Cooperative NOMA broadcasting/multicasting for low-latency and high-reliability 5G cellular V2X communications," *IEEE Internet Things J.*, vol. 6, no. 5, pp. 7828–7838, Oct. 2019.

[19] T. Nguyen, T. N. Do, and G. Kaddoum, "Performance analysis of multi-user NOMA wireless-powered mMTC networks: A stochastic geometry approach," *IEEE Trans. Commun.*, vol. 70, no. 11, pp. 7400–7417, Nov. 2022.

[20] Z. Ding, Z. Yang, P. Fan, and H. V. Poor, "On the performance of non-orthogonal multiple access in 5G systems with randomly deployed users," *IEEE Signal Process. Lett.*, vol. 21, no. 12, pp. 1501–1505, Dec. 2014.

[21] S. Goyal et al., "Full duplex cellular systems: Will doubling interference prevent doubling capacity?," *IEEE Commun. Mag.*, vol. 53, no. 5, pp. 121–127, May 2015.

[22] K. Mizutani and H. Harada, "Quantization noise reduction by digital signal processing-assisted analog-to-digital converter for in-band full-duplex systems," *IEEE Trans. Wirel. Commun.*, vol. 21, no. 8, pp. 6643–6655, Aug. 2022.

[23] A. Sabharwal et al., "In-band full-duplex wireless: Challenges and opportunities," *IEEE J. Sel. Areas Commun.*, vol. 32, no. 9, pp. 1637–1652, Sep. 2014.

[24] K. Mizutani, T. Matsumura, and H. Harada, "Comprehensive performance evaluation of universal Time-domain windowed OFDM-based LTE downlink system," *IEICE Trans. Commun.*, vol. E102-B, no. 8, pp. 1728–1740, Aug. 2019.

[25] Y. Medjahdi, D. le Ruyet, F. Bader, and L. Martinod, "Integrating LTE broadband system in PMR band: OFDM vs. FBMC coexistence capabilities and performances," in *Proc. IEEE 11th Int. Symp. Wireless Commun. Syst.*, 2014, pp. 643–648.

[26] V. Vakilian, T. Wild, F. Schaich, S. ten Brink, and J.-F. Frigon, "Universal-filtered Multi-carrier technique for wireless systems beyond LTE," in *Proc. IEEE Globecom Workshops*, 2013, pp. 223–228.

[27] Y. Ichikawa, K. Mizutani, and H. Harada, "Highly efficient OFDM applying symbol-edges truncating transmission technique," in *Proc. IEEE VTC-Fall*, 2022, pp. 1–5.

[28] M. Mohanmmadi, H. Q. Ngo, and M. Matthaiou, "Cell-free massive MIMO meets OTFS modulation," *IEEE Trans. Commun.*, vol. 70, no. 11, pp. 7728–7747, Nov. 2022.

[29] Y. Liu et al., "Multiband user equipment prototype hardware design for 5G communications in Sub-6-GHz band," *IEEE Trans. Microw. Theory Techn.*, vol. 67, no. 7, pp. 2916–2927, Jul. 2019.

[30] S. Handagala and M. Leeser, "Real time receiver baseband processing platform for sub 6 GHz PHY layer experiments," *IEEE Access*, vol. 8, pp. 105571–105586, 2020.

[31] 3GPP, "Physical channels and modulation," 3GPP Tech. Specification 38.211 V15.2.0, Jun. 2018.

[32] A. Omri, M. Shaqfeh, A. Ali, and H. Alnuweiri, "Synchronization procedure in 5G NR systems," *IEEE Access*, vol. 7, pp. 41286–41295, Mar. 2019.

[33] 3GPP, "Radio Resource Control (RRC); Protocol specification," 3GPP Tech. Specification 38.331 V15.7.0, Oct. 2019.

[34] "PXIe-1082 safety, environmental, and regulatory information," NI, Apr. 2022, Accessed: Aug. 31, 2022. [Online]. Available: https://www.ni.com/docs/ja-JP/bundle/pxie-1082-seri/resource/372752c.pdf

[35] 3GPP, "Base Station (BS) radio transmission and reception," 3GPP Tech. Specification 38.104 V15.16.0, Dec. 2021.

[36] "PXIe-6674T Specifications," NI, May 2022, Jul. 2022. Accessed: Aug. 31, 2022. [Online]. Available: https://www.ni.com/docs/ja-JP/bundle/pxie-6674t-specs/page/specs.html

[37] 3GPP, "User equipment (UE) radio transmission and reception; Part 1: Range 1 standalone," 3GPP Tech. Specification 38.101-1 V15.17.0, Mar. 2022.

[38] A. Sakai, K. Mizutani, T. Matsumura, and H. Harada, "Highly efficient sensing methods of primary radio transmission systems toward dynamic spectrum sharing-based 5G systems," *IEICE Trans. Commun.*, vol. E104-B, no. 10, pp. 1227–1236, Oct. 2021.

[39] P. H. Moose, "A technique for orthogonal frequency division multiplexing frequency offset correction," *IEEE Trans. Commun.*, vol. 42, no. 10, pp. 2908–2914, Oct. 1994.

[40] 3GPP, "Relay radio transmission and reception," 3GPP Tech. Specification 36.116 V11.4.0, Apr. 2015.

SHOTA MORI (Student Member, IEEE) received the B.E. degree in 2021 with the Faculty of Engineering, Kyoto University, Kyoto, Japan, where he is currently working toward the M.I. degree with the Graduate School of Informatics. His current research focuses on physical layer technologies of the 6th generation mobile communication (6G) system. He was the recipient of the Student Paper Award from IEEE VTS Tokyo/Japan Chapter in 2021 and Student Award from IEICE technical committee on SRW in 2022.

KEIICHI MIZUTANI (Member, IEEE) received the B.E. degree in engineering from the Osaka Prefecture University, Sakai, Japan, in 2007, and the M.E. and Ph.D. degree in engineering from the Tokyo Institute of Technology, Tokyo, Japan, in 2009 and 2012, respectively. He is currently an Associate Professor with the Graduate School of Informatics, Kyoto University, Kyoto, Japan. In 2010, he was an Invited Researcher with Fraunhofer Heinrich Hertz Institute, Berlin, Germany. From April 2012 to September 2014, he was a Researcher with the National Institute of Information and Communications Technology (NICT). From October 2014 to December 2021, he was an Assistant Professor with the Graduate School of Informatics, Kyoto University. From January 2021 to September 2022, he was an Associate Professor with the School of Platforms, Kyoto University. His current research interests include physical layer technologies in white space communications, dynamic spectrum access, wireless smart utility networks, and 4G/5G/6G systems, including OFDM, OFDMA, MIMO, multi-hop relay network, and full-duplex cellular systems. Since joining in NICT, he has been involved in IEEE 802 standardization activities, namely 802.11af, 802.15.4m and 802.22b. He was the recipient of the Special Technical Awards from IEICE SR technical committee in 2009 and 2017, Best Paper Award from IEICE SR technical committee in 2010 and 2020, Young Researcher's Award from IEICE SRW technical committee in 2016, Best Paper Award from WPMC2017 and WPMC2020, and Best Paper Presentation Award (1st Place) from IEEE WF-IoT 2020.

HIROSHI HARADA (Member, IEEE) is currently a Professor with the Graduate School of Informatics, Kyoto University, Kyoto, Japan, and a Research Executive Director of the Wireless Networks Research Center, National Institute of Information and Communications Technology (NICT). In 1995, he joined the Communications Research Laboratory, Ministry of Posts and Communications (currently, NICT). From 2005 to 2014, he was a Visiting Professor with the University of Electro-Communications, Tokyo, Japan. Since 1995, he has been researching on the topic of software defined radio, cognitive radio, dynamic spectrum access network, wireless smart ubiquitous network, and broadband wireless access systems on VHF, UHF, microwave, and millimeter-wave bands. In 2014, he was a Professor with Kyoto University. He has also joined many standardization committees and forums in U.S. and Japan and fulfilled important roles for them, especially IEEE 1900 and IEEE 802. He was the Chair of IEEE DySpan Standards Committee and Vice Chair of IEEE 802.15.4g, IEEE 802.15.4m, 1900.4, and TIA TR-51. He was the Board of Directors of IEEE communication society standards board, SDR forum, DSA alliance, and whitespace alliance. He is a Co-Founder of Wi-SUN alliance and was the Chairman of the Board. He is currently the Vice Chair of IEEE 2857, IEEE 802.15.4aa, and Wi-SUN alliance. He moreover was the Chair of the IEICE Technical Committee on Software Radio and Public Broadband Mobile Communication Development Committee, ARIB. He is also involved in many other activities related to telecommunications. He has authored the book entitled *Simulation and Software Radio for Mobile Communications* (Artech House, 2002). He was the recipient of the achievement awards in 2006 and 2018 and Fellow of IEICE in 2009, respectively and the achievement awards of ARIB in 2009, 2018, and 2022, respectively, on the topic of research and development on cognitive radio and wireless smart utility network.